T-Mart Theoretical Basis Document

Topography-Adjusted Monte Carlo Simulation of the Adjacency Effect in Remote Sensing of Coastal and Inland Waters

Yulun Wu

Requested by Liquid Geomatics

January 5 to March 15, 2022

Table of Contents

Summary

A three-dimensional (3D) radiative transfer code was developed to simulate top-of-atmosphere (TOA) reflectances of diverse aquatic environments such as coastal and inland waters. This code can be used to quantify the contribution of surrounding land towards the TOA reflectance of water pixels in spaceborne and airborne imagery — a phenomenon known as the adjacency effect. The model is named Topography-adjusted Monte-carlo Adjacency-effect Radiative Transfer code (T-Mart). T-Mart supports plane-parallel atmospheres and triangulated 3D surfaces with Lambertian and specular reflective properties, and it computes reflectances and irradiances with a difference of less than 0.6% compared to libRadtran. Preliminary results show that the topography of a vegetation-covered coastline has limited influence on the TOA reflectance of nearby waters. More analysis is needed to assess the effects of coastal topography and landcover types on aquatic remote sensing. This code will later be used to derive surface-level water reflectance from optical imagery and, ultimately, water properties such as chlorophyll concentration and water depth.

Introduction

Aquatic Remote Sensing

Aquatic remote sensing is the quantitative study of Earth's waterbodies such as oceans, rivers and lakes through their interactions with light (Mobley, 2020). The amount of radiation leaving the water surface, as captured by optical sensors, contains information about the biophysical properties of the water, such as chlorophyll concentration, turbidity and water depth (Lee et al., 1998). Optical measurements of natural waters made from aircraft and satellites have been studied intensively to derive these properties in the past decades (Kutser et al., 2020; Palmer et al., 2015).

While operational monitoring of the ocean is nowadays established using a variety of sensors such as NASA's Moderate Resolution Imaging Spectroradiometer (MODIS) and ESA's Sentinel-3 Ocean and Land Color Instrument (OLCI), determination of the optical properties of coastal and inland waters remains a challenge due to their more diverse constituents and complex optical environments (Bulgarelli & Zibordi, 2018). The land surrounding waters can influence the light intensity or radiance of the water captured by satellite sensors and negatively affect the accuracy of remote-sensing products (illustrated in Figure 2). The influence of adjacent objects on the top-of-atmosphere (TOA) radiance of the target is termed the adjacency effect.

The TOA radiance of an ocean surface can be broken down into the following components:

$$L_t = L_{atm} + L_{surf} + L_w \qquad\qquad \text{Eq. 1}$$

where L_t is the total radiance measured by the sensor, L_{atm} is atmospheric intrinsic radiance (light reflected by the atmosphere), L_{surf} is radiance resulting from specular reflectance of the

water surface, also known as sunglint, and L_w is the water-leaving radiance that comes from below the water surface (Moses et al., 2017). Out of the three radiances, L_w is the only one that contains information about the biophysical parameters of the underlying water; as a result, isolating L_w from L_t becomes an essential prerequisite to deriving quantitative estimates of water properties from remote-sensing data (Moses et al., 2017). We can see in Figure 1, which shows the simulated TOA radiance for a typical marine environment, that L_w contributes 10% or less of the TOA radiance in the visible range and is negligible in the longer wavelengths. The low contribution of L_w to L_t highlights the importance of accurately modelling L_w in diverse optical conditions (e.g., various solar angles and water turbidity) before establishing algorithms that derive L_w from L_t, a process called atmospheric correction.
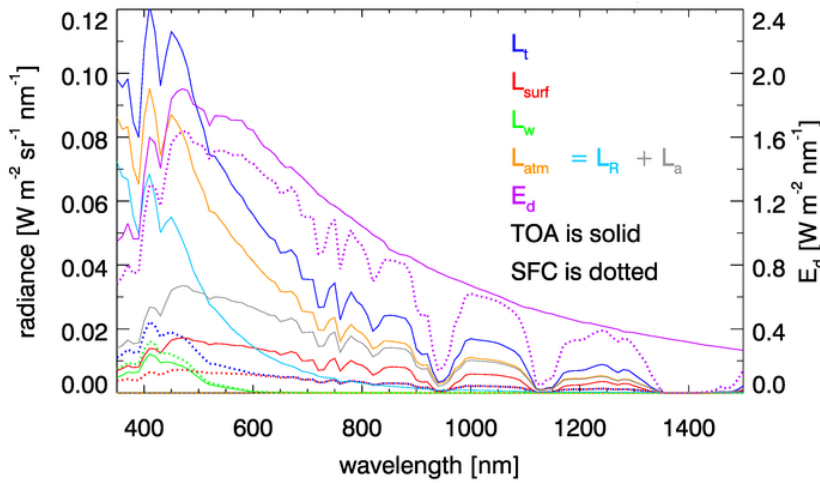

Figure 1. TOA radiance of a typical ocean-ocean scene. Solid lines represent TOA radiances; dotted lines are at the sea surface. L_R and L_a are atmospheric intrinsic radiance from Rayleigh scattering and aerosol scattering, respectively. E_d is downward irradiance. Source: Mobley (2021b).

The TOA radiance (i.e., the brightness of an area measured from space) of an object largely depends on its illumination condition, i.e., an object may appear dark at night not because it is not reflective but because of a lack of sunlight. Due to the rapidly varying illumination conditions because of changes in the sun's position and cloud/aerosol distributions, in optical remote sensing, it is almost always the reflectance (R) of an object that provides information about the object. R is calculated as the product of radiance and a bidirectional reflectance distribution function (BRDF) correction coefficient, a term that describes the angular distribution of reflected light. For a Lambertian surface (a surface that reflects light isotropically or evenly towards all directions, e.g., a piece of paper is close to Lambertian as its brightness varies very little as you change the viewing direction), the BRDF correction coefficient is π, making it $R = L \times \pi / E$ (Table 1).

In the presence of a scattering atmosphere, light reflected off the surrounding area can reach the satellite sensor as diffuse radiance through multiple scattering (Figure 2b). The increased TOA reflectance of the water surface in the view of the sensor (thickened line in Figure 2b) is referred to as adjacency radiance. Note that adjacency radiance can be negative when the target is adjacent to a surface less reflective than itself.
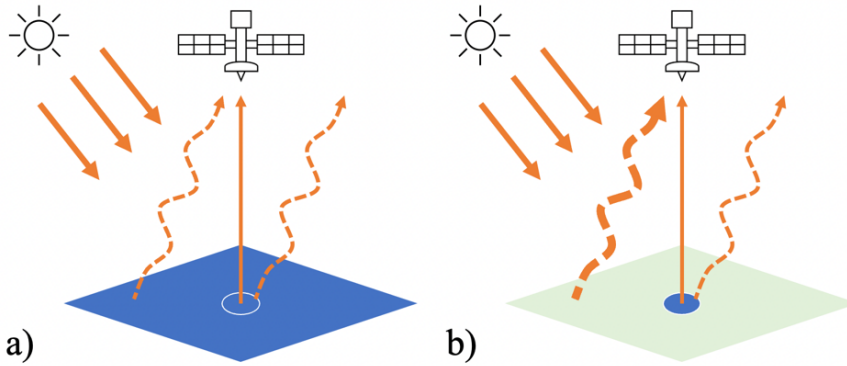
Figure 2. TOA radiance received by satellite sensors from a) an open ocean and b) a waterbody (blue circle) adjacent to land (green). Solid and dashed arrows from the surface are direct and diffuse radiance, respectively. Thickness of lines represents radiance intensity.

The adjacency effect distorts the colour or the spectral shape of water pixels in remotely sensed TOA imagery, and often leads to a failure to isolate L_w from L_t, undermining the accuracy of retrieved water properties (Sterckx et al., 2011). While a few studies investigated removing the adjacency effect from TOA reflectance of water surfaces (Kiselev et al., 2015; Sei, 2015; Sterckx et al., 2011), the majority of ocean-colour data processors assume a homogenous underlying surface (Bulgarelli & Zibordi, 2018). Detailed modelling and assessment of the adjacency effect and general solutions for correcting them are therefore required to advance operational monitoring from open oceans to coastal and inland waters.

Monte Carlo Radiative Transfer Modelling

The movement and attenuation of electromagnetic radiation across various media are modelled extensively in radiative transfer (RT) codes such as 6S (Vermote et al., 1997), libRadtran (Emde et al., 2016) and HydroLight (Mobley & Sundman, 2008). However, when considering arbitrary boundary geometry and significant multiple scattering, and with an arbitrary distribution of optical properties within the media, general techniques become insufficient and Monte Carlo methods often become the only feasible option (Gordon, 1985). As a result, this study uses the Monte Carlo approach to simulate TOA reflectances affected by the adjacency effect.

In RT modelling, Monte Carlo relies on repeated random sampling of photons' scattering and propagation directions following the specified probability distributions. Photons are released at the light source and are traced all the way to the detector or sensor. The ratio of the number of released and collected photons at different locations and directions can be used to infer the optical properties of the medium and the reflective surfaces.

Monte Carlo methods have the advantage of accurately modelling multiple scattering and multiple reflection effects (Tanre et al., 1981). Although computationally expensive, Monte Carlo is commonly used to look at the adjacency effect from neighbouring surfaces and to derive the degree and extent of the adjacency effect for circular targets under different atmospheric conditions (Reinersman & Carder, 1995; Tanre et al., 1981; Vermote et al., 1997).

4

The adjacency effect is more significant in environments with a high contrast of reflective properties; for example, the TOA reflectance of water is often influenced by the nearby land in coastal and inland environments because land and vegetation usually have much higher reflectance than waters. To accurately model the adjacency effect in coastal and inland remote sensing, the scattering and absorptive properties of the atmosphere in three dimensions and the reflective properties of the surfaces must be considered. Bulgarelli et al. (2014) modelled the adjacency effect in a coastal environment through a Monte Carlo approach: a single atmosphere profile with molecular and aerosol optical properties was implemented, flat land and water surfaces were assumed, and the wind-induced rough sea surface was modelled through an analytical expression. This study builds on Bulgarelli et al. (2014), utilizes the rich library of atmosphere and aerosol profiles in an existing software package and considers the effects of elevation and landscape topography to further assess the impact of the adjacency effect in aquatic remote sensing.

Table 1. Radiative quantities and their symbols and units.

Name	Symbol	Unit
Radiant flux	Φ	Watts or joules per second
Radiance	L	Watts per steradian per square meter (W sr^{-1} m^{-2})
Irradiance and exitance	E	Watts per square meter (W m^{-2})
Reflectance	R	Non-dimensional, radiance-calculated reflectance: $R = L \times \pi / E$
Irradiance reflectance	R (E/E$_0$)	Non-dimensional, calculated as exitance over irradiance

Table 2. Glossary of terms.

Name	Definition
Absorption coefficient	The ability of a medium to absorb the radiant flux of a beam as it passes through the medium, in unit of m^{-1}
Scattering coefficient	The ability of a medium to scatter the radiant flux of a beam as it passes through the medium, in unit of m^{-1}
Scattering phase function	The angular distribution of light scattered by molecules or particles
Extinction coefficient	The ability of a medium to absorb **AND** scatter the radiant flux of a beam as it passes through the medium, in unit of m^{-1}
Optical thickness or optical depth (τ)	The thickness of the medium multiplied by its absorption/scattering/extinction coefficient; quantifies the amount of radiant flux
Asymmetry parameter	The tendency of scattering particles to scatter radiation to the front or back preferentially
Scale height	Describing the rate of decrease of concentration with altitude; defined as the distance over which the concentration decreases by a factor of e

Objectives

This study aims to accurately model the radiative transfer between satellite sensors and water surfaces in complex landscapes and under different atmospheric conditions using the Monte Carlo approach, assess the effects of topography on aquatic remote sensing, and ultimately lay the foundation for physics-based adjacency-correction methods.

Methods

Overview

A Monte-Carlo RT code was developed in Python to simulate photons' propagation and attenuation from the TOA to Earth's surface and back to the top of the atmosphere. It utilizes the *multiprocessing* package in Python to speed up calculations. Collimated solar irradiance is the light source and the sensor is set as an arbitrary point in this three-dimensional (3D) space. A backward Monte-Carlo approach is used, i.e., photons are released from the sensor and they propagate towards the target pixel as their initial moving direction. Photons are scattered, reflected and attenuated according to their propagation paths and the optical properties of the media and the reflecting surfaces. Photons are tallied when they exit the top of the atmosphere to infer the optical properties of the atmosphere-ocean system. The code supports fully 3D topography and is named Topography-adjusted Monte-carlo Adjacency-effect Radiative Transfer code (T-Mart).

T-Mart limits its scope to wavelengths between 0.3 and 1.5 μm where diatomic oxygen molecules (O_2), ozone (O_3) and water vapour are usually the only strong absorbers. This meets the requirements for aquatic optical remote sensing which relies mostly on visible and near-infrared wavelengths. Clouds and polarization are not considered in this study.

Atmosphere

By default, the modelled atmosphere is divided into 20 horizontally homogeneous layers. Each layer has its unique absorption and scattering properties according to its aerosol and molecule composition which is directly imported from 6S through the Py6S interface (Wilson, 2013). There are six aerosol models included in 6S: continental, maritime, urban, desert, biomass burning and stratospheric. Each model has its unique wavelength-dependent extinction coefficient, scattering albedo, asymmetry parameter and scattering phase function. There are also six atmosphere models in 6S: midlatitude summer, midlatitude winter, subarctic summer, subarctic, tropical and U.S. standard. Each of them has its vertical distribution of water vapour and ozone gases. The concentration of aerosols and other molecules in each atmospheric layer is determined by pre-specified scale heights. By default, the scale heights are 8km for molecules and 2km for aerosol particles.

Scattering and Absorption

A photon's movement starts with a specified initial position and an initial direction. An optical thickness for scattering, τ_{scat}, is sampled following Mayer (2009),

$$\tau_{scat} = -\ln(\Re) \qquad \text{Eq. 2}$$

where $\Re$ is a random number evenly distributed between 0 and 1. Then an end position of this straight-line movement is determined by integrating the scattering coefficient along the propagation direction until we have reached the τ_{scat} determined by Eq. 2:

$$\tau_{scat} = \sum_{layers} l_i \cdot k_{scat\,i} \qquad \text{Eq. 3}$$

where l_i is the length that the photon travels in layer i, and $k_{scat\,i}$ is the scattering coefficient of that layer. This is essentially stacking the layers in the photon's direction of propagation and determining the number of layers it takes to "consume" the sampled τ_{scat}. Note that because of the random nature of $\Re$, the end position is almost never at the boundary between two atmospheric layers.

There are three scenarios that can happen after the photon's movement:
1) **The end position is below the surface**. In this case, we trace the intersecting point between the surface and the straight line formed by the movement's initial and end positions, and use the intersecting point as the new initial position for the next movement (see section Surface and Reflection).
2) **The end position is above the TOA**. Then the simulation for this photon is ended and radiative quantities are calculated (see section Calculating Radiative Quantities). New photons are then launched until T-Mart reaches the specified sample size.
3) **The end position is in the atmosphere**. A scattering mode (either aerosol or Rayleigh scattering) is sampled using the ratio of the two scattering coefficients. A new propagation direction is then determined according to the scattering phase function of the sampled scattering mode.

The absorption of light in the atmosphere is simulated through a weight system. The photon carries a weight of 1 when it enters the atmosphere, and the weight changes according to its movement paths and the absorption coefficients of the atmospheric layers and the surface.

Regardless of the scenarios above, an absorption optical thickness is calculated similar to Eq. 3,

$$\tau_{abs} = \sum_{layers} l_i \cdot k_{abs\,i} \qquad \text{Eq. 4}$$

where $k_{abs\,i}$ is the absorption coefficient of layer i. For movements that stopped before "consuming" the entire sampled τ_{scat} (scenarios 1 and 2 above), τ_{abs} is calculated from the

initial position only to the intercepting point at TOA or the surface, not to the end position. Then the direct transmittance for absorption can be calculated as

$$T_{abs} = e^{-\tau_{abs}}$$

<div align="right">Eq. 5</div>

using which we can simulate the antennation of light as it travels through the medium by modifying the photon's weight (w),

$$w = w_0 \cdot T_{abs}$$

<div align="right">Eq. 6</div>

where w_0 is the photon's weight before the movement. To differentiate different components of TOA reflectance, the number of scattering and reflection events that happened to each photon is recorded throughout all its movements.

Surface and Reflection

Triangulation

When the line formed by the photon's movement intersects a pixel, the photon is reflected from the point of intersection (Figure 3). A new weight of the photon is calculated by multiplying the initial weight by the reflectance of the surface (R_{surf}). In order to properly model the effects of elevation and landscape morphology on TOA reflectance, the pixels of a digital elevation model (DEM) are connected to form 3D triangles (Figure 3). This enables modelling of RT in complex topography.
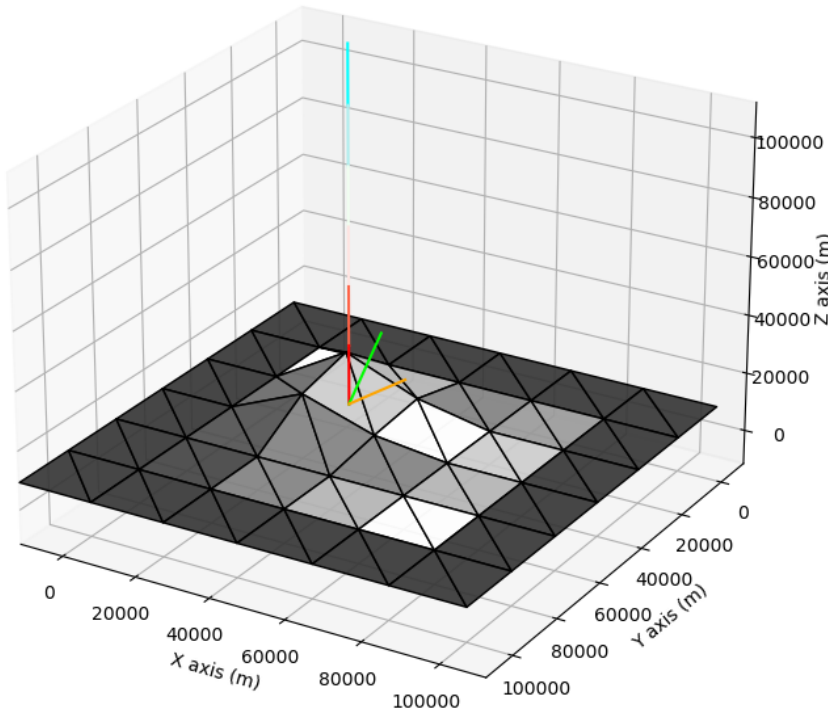

Figure 3. Illustration of a photon incident on a triangulated surface. The photon moves from the blue end to the red end of the vertical line and intersects the triangulated pixel below. The green

<div align="center">8</div>

line intersecting the same point is the surface normal of the triangle. The orange line is the sampled direction from a reflection of a Lambertian surface tilted to the surface normal, it is also the new direction of propagation in the photon's next movement.

When a photon intercepts the triangulated surface, a new direction of propagation is sampled following the BRDF of the surface, and the new direction is tilted to the surface normal of the triangle (Figure 3).

For every photon movement, the line formed by the movement is tested for intersection with the triangles. When the photon reaches the surface outside the DEM, it is reflected by the background surface. The background surface can be separated into two sections divided by a straight line; each section has its own reflectance, and each extends horizontally to infinity as a homogeneous and Lambertian surface. This is to facilitate the modelling of coastal environments where two background reflectances are needed.

A few reflectance spectra were incorporated in T-Mart in the preliminary version, and they include soil, vegetation and water (Figure 4).
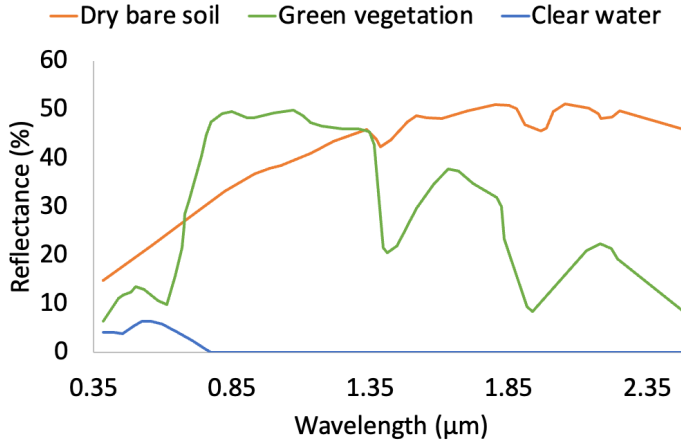

Figure 4. Typical reflectance spectra of selected land covers, modified from SEOS (n.d.).

Cox-Munk Slope Statistics

Cox-Munk sea surface slope statistics (Cox & Munk, 1954) are widely used in aquatic remote sensing to model the sea-surface status and the angular distribution of its specular reflectance. T-Mart uses a version of Cox-Munk slope statistics modified by Mobley (2021a), and it is described as follows.

In a wind-cantered coordinate system, let $\eta(x_a, x_c)$ be the sea surface elevation where x_a is the coordinate along the wind direction and x_c in the cross-wind direction. Then the sea surface slopes in these two directions, η_a and η_c, can be described as

$$\eta_a = \frac{\partial \eta}{\partial x_a} \text{ and } \eta_c = \frac{\partial \eta}{\partial x_c}. \qquad \text{Eq. 7}$$

Cox and Munk approximated the slopes of the sea surface as a function of wind speed and wind direction following a bivariate Gaussian distribution:

$$p(\eta_a, \eta_c) = \frac{1}{2\pi\sigma_a\sigma_c} \exp\left[-\frac{1}{2}\left(\frac{\eta_a^2}{\sigma_a^2} + \frac{\eta_c^2}{\sigma_c^2}\right)\right]$$

Eq. 8

where the two variances (σ_a along and σ_c across wind direction) are calculated using the wind speed U (m/s) at 12.5m from the surface,

$$\sigma_a^2 = 3.16 \cdot 10^{-3} U$$
$$\sigma_c^2 = 1.92 \cdot 10^{-3} U$$

Eq. 9

Note that the probability distribution function $p(\eta_a, \eta_c)$ is normalized so that integrating both directions to infinity gives a value of 1,

$$\int_{-\infty}^{\infty}\int_{-\infty}^{\infty} p(\eta_a, \eta_c)d\eta_a\, d\eta_c = 1.$$

Eq. 10

Fresnel's Equations for Unpolarized Light

The law of refraction (also known as Snell's law) states that,

$$n_1 \sin\theta_1 = n_2 \sin\theta_2$$

Eq. 11

where n_1 and n_2 are the refractive indices of two media, and θ_1 and θ_2 are interchangeably angle of incidence and angle of transmission. The refractive indices of air (n_a) and water (n_w) are usually taken as 1 and 1.34 at visible wavelengths.

When light is incident on the water from the air, the angle of transmission (θ_t) is a function of the incident angle (θ_i) and the refractive indices of the two media,

$$\theta_t = \sin^{-1}(\frac{n_w}{n_a}\sin\theta_i).$$

Eq. 12

The fraction of this incident irradiance reflected directly by the air-water interface (i.e. not penetrating the surface) is then described by Fresnel's equation,

$$R(\theta_i) = \frac{1}{2}\left\{\left[\frac{\sin(\theta_i - \theta_t)}{\sin(\theta_i + \theta_t)}\right]^2 + \left[\frac{\tan(\theta_i - \theta_t)}{\tan(\theta_i + \theta_t)}\right]^2\right\}$$

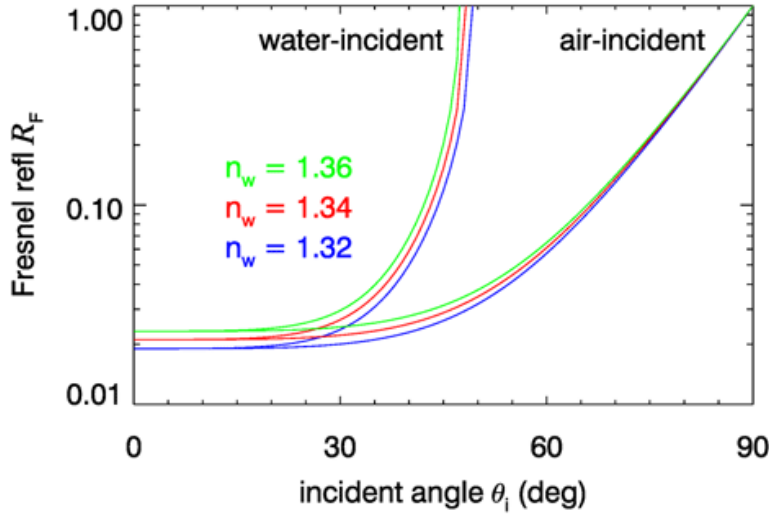Eq. 13

and this is plotted in Figure 5.

Figure 5. Fresnel reflectance as a function of incident angles for unpolarized light and selected refractive indices of water (Mobley, 2021c).

Whitecaps

Whitecaps are the foamy crests of waves at the water surface. T-Mart uses an empirical equation, taken from Mobley (2021d), to simulate the contribution of whitecaps to the TOA reflectance. Whitecap reflectance is assumed to be Lambertian, and it is calculated as

$$R_{wc}(\lambda) = a_{wc}(\lambda) \times 0.22 \times F_{wc} \qquad \text{Eq. 14}$$

where F_{wc} is the fraction of the sea surface covered by whitecaps:

$$F_{wc} = 8.75 \times 10^{-5}(U_{10} - 6.33)^3 \qquad \text{Eq. 15}$$

and $a_{wc}(\lambda)$ is a correction factor that describes the wavelength dependence of reflectance from whitecaps (Table 3).

Table 3. Spectral dependency of whitecap reflectances, source: Frouin et al. (1996).

Wavelength	Value
400	1
444	1
543	0.95
663	0.92
871	0.62
1023	0.53
1654	0.14

$$R_{water} = R_{wc} + (1 - F_{wc}) \times (R_{surface} + R_{water-leaving\ 0+}) \qquad \text{Eq. 16}$$

To summarize, T-Mart currently has two BRDF models: 1) Lambertian surfaces that reflect light isotopically and 2) specular reflectance following Cox-Munk slope distribution and Fresnel's equations. Note that the reflectance of water has both Lambertian and specular components: water leaving and whitecap reflectances are Lambertian and surface reflection is specular (Eq. 16). These two are weighted according to their reflectance values when calculating the propagation direction and the new photon weight after reflecting off the water surface.

Backward Monte Carlo Method

T-Mart is a backward Monte Carlo model, meaning that it launches photons from the sensor and traces it back to the sun. In regular (forward) Monte Carlo methods, simulated photons are released from the light source and are collected by a simulated instrument at a specified location. In the field of aquatic remote sensing, the light source is the parallel solar irradiance incident on the top of the atmosphere and the simulated sensor is located at a point of a satellite orbit. The problem associated with this is that the instrument is often very small compared to Earth's atmosphere and ocean system. As a result, the probability of a photon intercepting the instrument is extremely low, making the modelling impractical or highly inefficient (Mobley, 1994b). In addition, when simulating three-dimensional scenarios, the area of the surface receiving photons cannot be determined in advance because this depends on sun-earth-sensor geometries and environmental conditions such as the scattering properties of the atmosphere (Mobley, 1994b).

Backward Monte Carlo models are often used to overcome the challenges posed in forward Monte Carlo models (Bulgarelli et al., 2014; Reinersman & Carder, 1995). Instead of releasing the photons at the light source, backward models release photons at the sensor and trace them all the way to the light source. This approach overcomes the difficulties of releasing photons at a surface with unknown size and collecting photons at a point target, and because almost all released photons are tallied, this also improves computational efficiency significantly (Mobley, 1994b). Backward Monte Carlo methods rely on the principle of reciprocity in radiative transfer (Light, 2003), i.e., the same amount of photons will be received at the sensor if the sensor and the light source switch places.

Calculating Radiative Quantities

T-Mart is capable of calculating two types of radiative quantities: 1) ratios of radiant irradiance/exitance to irradiance and this includes irradiance reflectance, and 2) radiance-calculated reflectances (see calculation in Table 1). The former does not consider the angular distribution of the reflected light but plays an important role in determining the illumination conditions of surfaces and atmospheric particles. The latter is more commonly used in remote sensing as we usually derive the reflectance of a surface by observing from a single fixed angle (aperture of the sensor) and assuming Lambertian reflectance (e.g., light is equally intense in other directions). The assumption of Lambertian reflectance can often be violated, e.g., when seeing sunglint on the water surface, leading to unrealistic radiance-calculated reflectances, and that is why a specular BRDF model is essential for modelling water's optical properties.

The ratios of irradiance and exitance (output) to irradiance (input) at TOA or any elevation of the atmosphere are calculated by counting photons hitting or moving across a plane-parallel surface, weighted by the photons' weights,

$$E/E_0 = \frac{\sum_{photon} \sum_{movements} w}{N_{photon}} \qquad \text{Eq. 17}$$

where E is the output irradiance or exitance and E_0 is the input irradiance. As seen from Eq. 17, a photon can contribute to the irradiance or exitance at a certain level more than once through multiple scattering; i.e., photons reflected by the surface can be redirected to the surface again by molecules and aerosols in the atmosphere, increasing the amount of radiance that a surface receives. This phenomenon is called the spherical albedo.

Radiance is calculated using a method called the local-estimate technique (Marchuk et al., 1980). At every collision (scattering and reflection), the probability that a photon scatters into the sensor's direction is calculated using the scattering phase function of the sampled scattering mode, the remaining weight of the photon, and the extinction coefficient between collision and detector. The local-estimate weight, w_L, is then added to the total reflectance,

$$w_L = w_0 \cdot \frac{p(\theta_p) \cdot e^{-\tau_{exp}}}{\cos(\theta_s)} \qquad \text{Eq. 18}$$

where w_0 is the photon's weight, θ_p is the angle between the photon's propagation direction (before scattering) and the sensor's direction, and the phase function $p(\theta_p)$ describes the probability that the scattered angle is θ_p. This technique is analogous to creating a virtual photon at each collision point and forcing it to move towards the sensor (weighted by its probability to actually do so to achieve unbiased results). Just like the regular photons, the virtual photon is subject to extinction along its way to the sensor: a direct transmittance for extinction, $e^{-\tau_{exp}}$, is calculated similarly to what is in Eq. 5. Then, θ_s is the solar zenith angle to account for the slant distance of photons travelling in the atmosphere and the increased probability of scattering into the sensor. Finally, the total reflectance can be calculated as,

$$R = \frac{\sum_{photon} \sum_{movements} w_L}{N_{photon}}. \qquad \text{Eq. 19}$$

Again, a photon can contribute to the radiance-calculated reflectance multiple times to fully account for multiple scattering in the atmosphere.

The TOA reflectance in Eq. 19, R, can be divided into three components following 6S (Vermote et al., 2006),

Direct reflectance (R_{dir}): $n_{scatter} = 0$
Environmental reflectance (R_{env}): $n_{surface} \geq 1$ and $n_{scatter} \geq 1$
Atmospheric intrinsic reflectance (R_{atm}): $n_{surface} = 0$

13

where $n_{surface}$ and $n_{scatter}$ are respectively the number of surface reflections and scattering that happened to the photon. Note that $n_{scatter}$ resets to 0 each time the photon reaches a surface because any scattering events that happened to the photon before reaching the last surface are viewed as a spherical-albedo contribution to the surface irradiance. In other words, direct reflectance is from photons that travel from the target pixel to the sensor without being scattered (regardless of the photons' history before hitting the target pixel!), environmental reflectance is from photons that travel from the neighbouring pixels to the sensor through scattering, and atmospheric intrinsic reflectance is from photons that never reached the surface of the earth. Changes in environmental reflectance due to inhomogeneous surfaces is the basis of the adjacency effect.

Radiance, irradiance and exitance (the **non-ratio, absolute** radiative quantities) can be calculated by multiplying the ratios and reflectances by the irradiance at TOA. This is currently not supported by T-Mart because our main interest is reflectances as they are not affected by illumination conditions, but can be included in the future if needed because solar irradiance as a function of day-of-the-year, time-of-the-day and changes in Earth's orbit is well documented and relatively easy to implement.

Validation

With libRadtran

libRadtran (Mayer & Kylling, 2005) is a widely used software package for earth-observation radiative transfer calculations. It is open-source and written in Fortran and C. libRadtran supports the calculations of radiances, irradiance and actinic fluxes given atmospheric and surface parameters. Some of its applications include studying the radiative effects of greenhouse gases (Ehret et al., 2008) and aerosols from burning emissions (Saleh et al., 2015), and mapping the leaf area of seagrasses and their depth in the water (Hedley et al., 2016). Due to its versatility and recognition, libRadtran is selected to validate the results from T-Mart.

There are six radiative-transfer-equation (RTE) solvers in the publicly available version of libRadtran, each with its own specialties. MYSTIC and DISORT are among the most used solvers. Like T-Mart, MYSTIC is based on Monte Carlo random sampling. DISORT, on the other hand, is based on the method of discrete ordinates which approximates the almost unsolvable integrodifferential RTE by discretizing the infinite number of possible angles in a 3D space. This transforms the RTE into a system of linear differential equations, allowing quick and accurate calculations (although unable to incorporate arbitrary boundaries like Monte-Carlo-based models do). DISORT is the default solver of libRadtran.

MYSTIC has a 3D version that would ideally be used as the benchmark in this study due to its similar nature to T-Mart, but it is unavailable to the public (only a one-dimensional version is provided). DISORT is then used as the benchmark, provided that MYSTIC and DISORT

produce almost identical results (Mayer, 2009) and it does not have statistical noise from Monte Carlo simulations.

Validations of T-Mart against DISORT were run with molecular-scattering optical thicknesses from 0.05 to 0.5 in the absence of aerosols. This range is similar to the molecular-scattering optical thicknesses from 400 to 700nm which starts at approximately 0.36 at 400nm and decreases with longer wavelengths. Although wavelengths and molecular-scattering optical thicknesses are well correlated, optical thickness is used as the unit for comparison to show more gradual changes. R_{surf} is set as 0.1 for all validation runs below.
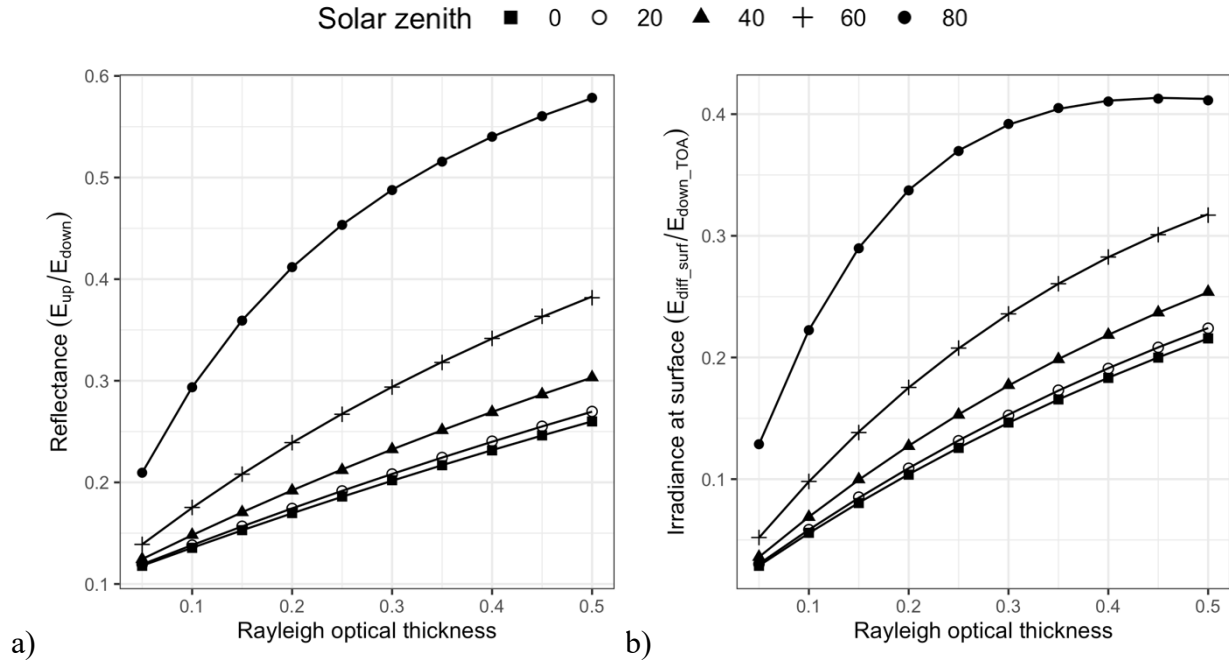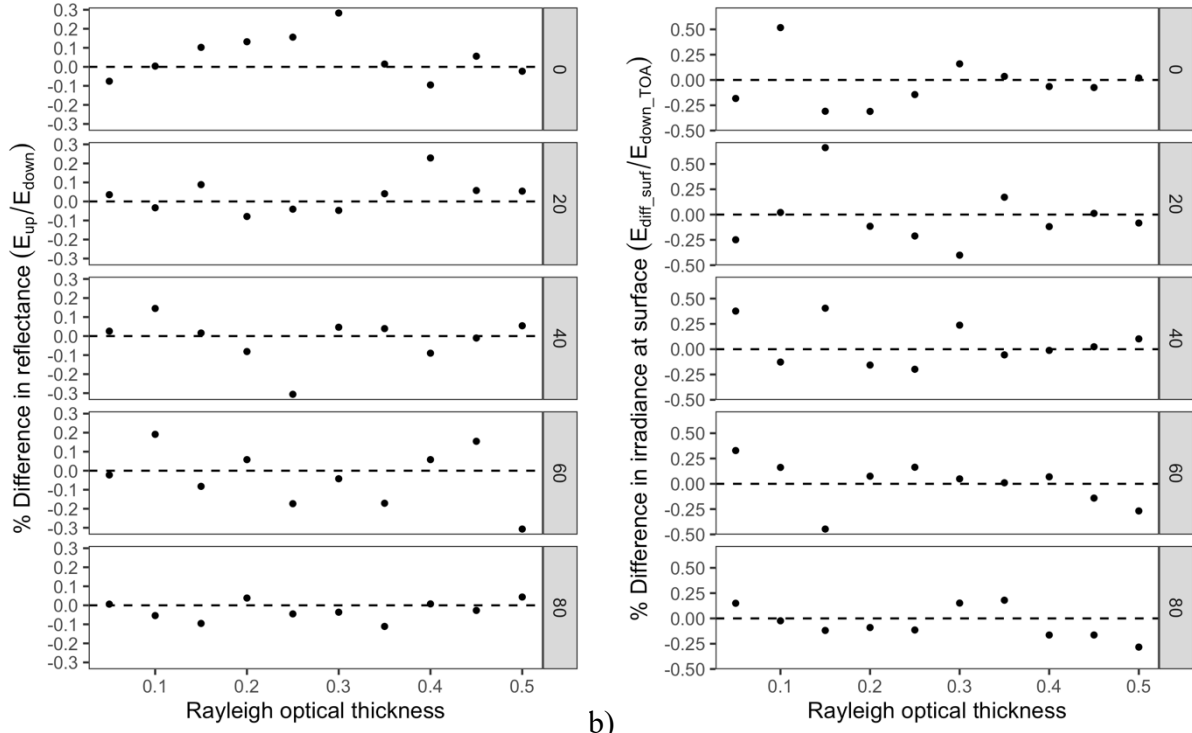

a)   b)

Figure 6. a) Irradiance reflectance at TOA, and b) the ratio of diffuse irradiance at surface level to total irradiance at TOA, both as a function of molecular-scattering optical thickness at selected solar zenith angles. Lines are from libRadtran DISORT, points (in various shapes) are from T-Mart. Nadir viewing angle, R_{surf} = 0.1, N_{photon} = 1,000,000, τ_{abs} = 0 (i.e., no absorption in the atmosphere).

The TOA irradiance reflectance and the ratio of diffuse irradiance at surface to total TOA irradiance calculated by T-Mart and DISORT are highly similar (Figure 6 and Table 4). Their differences are calculated as

$$\% \, difference = \frac{VALUE_{T-Mart} - VALUE_{DISORT}}{VALUE_{DISORT}} \times 100 \qquad \text{Eq. 20}$$

and the % differences and mean % differences are presented in Figure 7 and Table 4 respectively. The maximum mean % difference for a no-absorption atmosphere is 0.059% (Table 4), confirming the accuracy of T-Mart in calculating radiative quantities.

15

Figure 7. % Differences between T-Mart and libRadtran DISORT in calculated a) irradiance reflectance at TOA and b) ratio of diffuse irradiance at surface level to total irradiance at TOA, both as a function of molecular-scattering optical thickness at selected solar zenith angles. Nadir solar angle, $R_{surf} = 0.1$, $N_{photon} = 1,000,000$, $\tau_{abs} = 0$.

Table 4. Mean % differences in Figure 7.

Solar zenith	Reflectance (E/E_0)	Irradiance (E/E_0)
0	0.055	-0.036
20	0.031	-0.031
40	-0.016	0.059
60	-0.034	0.000
80	-0.027	-0.048

Next, with a smaller Monte Carlo sample size ($N_{photon} = 10,000$), the radiance-calculated reflectances were computed (Figure 8) with the same setting as in Figure 6. Ten thousand photons roughly take 30 seconds to run, providing a complete set of atmospheric intrinsic, direct and environmental reflectances (four vertically aligned points in Figure 8). Fewer photons were used to test the performance of T-Mart when computation time is of concern. T-Mart results still generally align with results from DISORT but with noticeable Monte Carlo simulation noise (Figure 8).
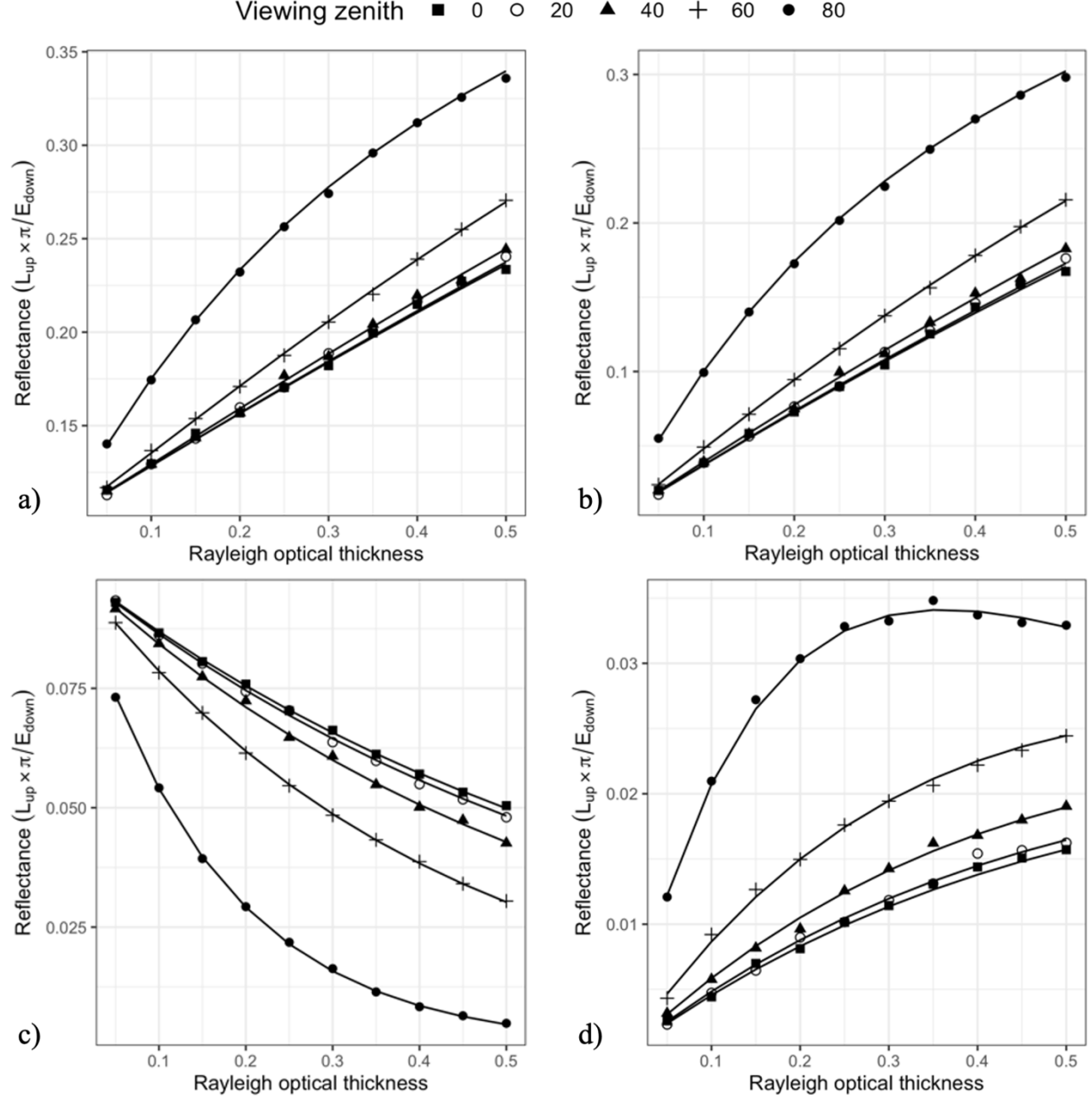
Figure 8. a) Total, b) atmospheric intrinsic, c) direct and d) environmental reflectances at TOA as a function of molecular-scattering optical thickness at selected view zenith angles. Lines are from libRadtran DISORT, shapes are from T-Mart. Nadir solar angle, $R_{surf} = 0.1$, $N_{photon} = 10,000$, $\tau_{abs} = 0$.

All the results above are based on atmospheres with no absorbance; next, we run the same analysis for the same one-layer atmosphere, but with an absorption optical thickness of 0.3, and calculate the same statistics for differences. Note that the $\tau_{abs} = 0.3$ leads to a direct transmittance of approximately 74%, this is an extremely hazy atmosphere and in practice wavelengths with this amount of absorption are avoided in ocean and land earth observations. Nevertheless, the extreme values help validate T-Mart results.
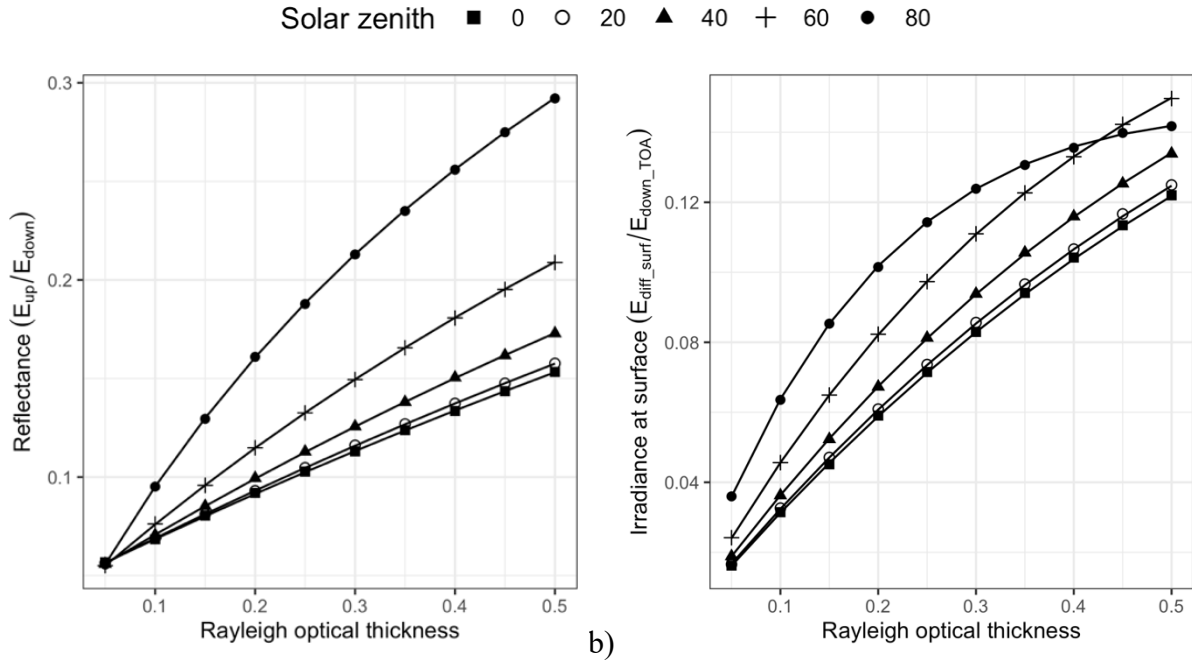
Figure 9. a) Irradiance reflectance at TOA, and b) the ratio of diffuse irradiance at surface level to total irradiance at TOA, both as a function of molecular-scattering optical thickness at selected solar zenith angles. Lines are from libRadtran DISORT, shapes are from T-Mart. Nadir viewing angle, $R_{surf} = 0.1$, $N_{photon} = 1,000,000$, $\tau_{abs} = 0.3$.
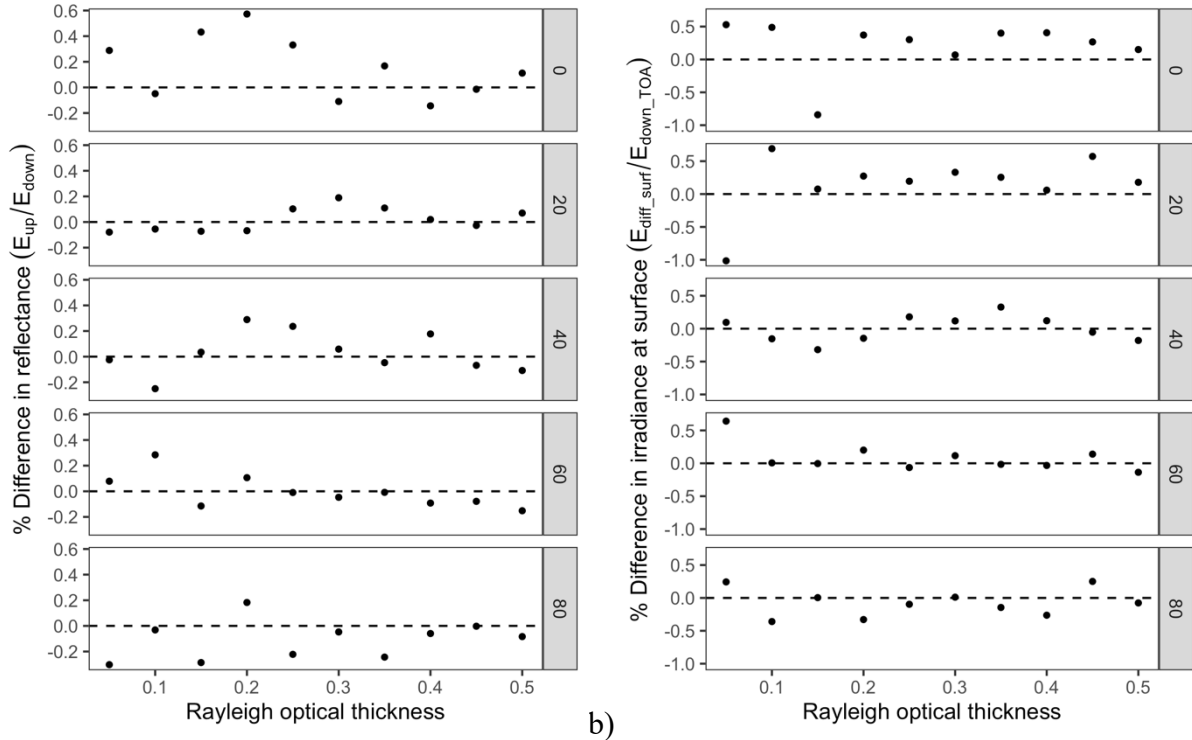

Figure 10. % Differences between T-Mart and libRadtran DISORT in calculated a) irradiance reflectance at TOA and b) ratio of diffuse irradiance at surface level to total irradiance at TOA,

both as a function of molecular-scattering optical thickness at selected solar zenith angles. Nadir solar angle, R_{surf} = 0.1, N_{photon} = 1,000,000, τ_{abs} = 0.3.

Table 5. Mean % differences in Figure 10.

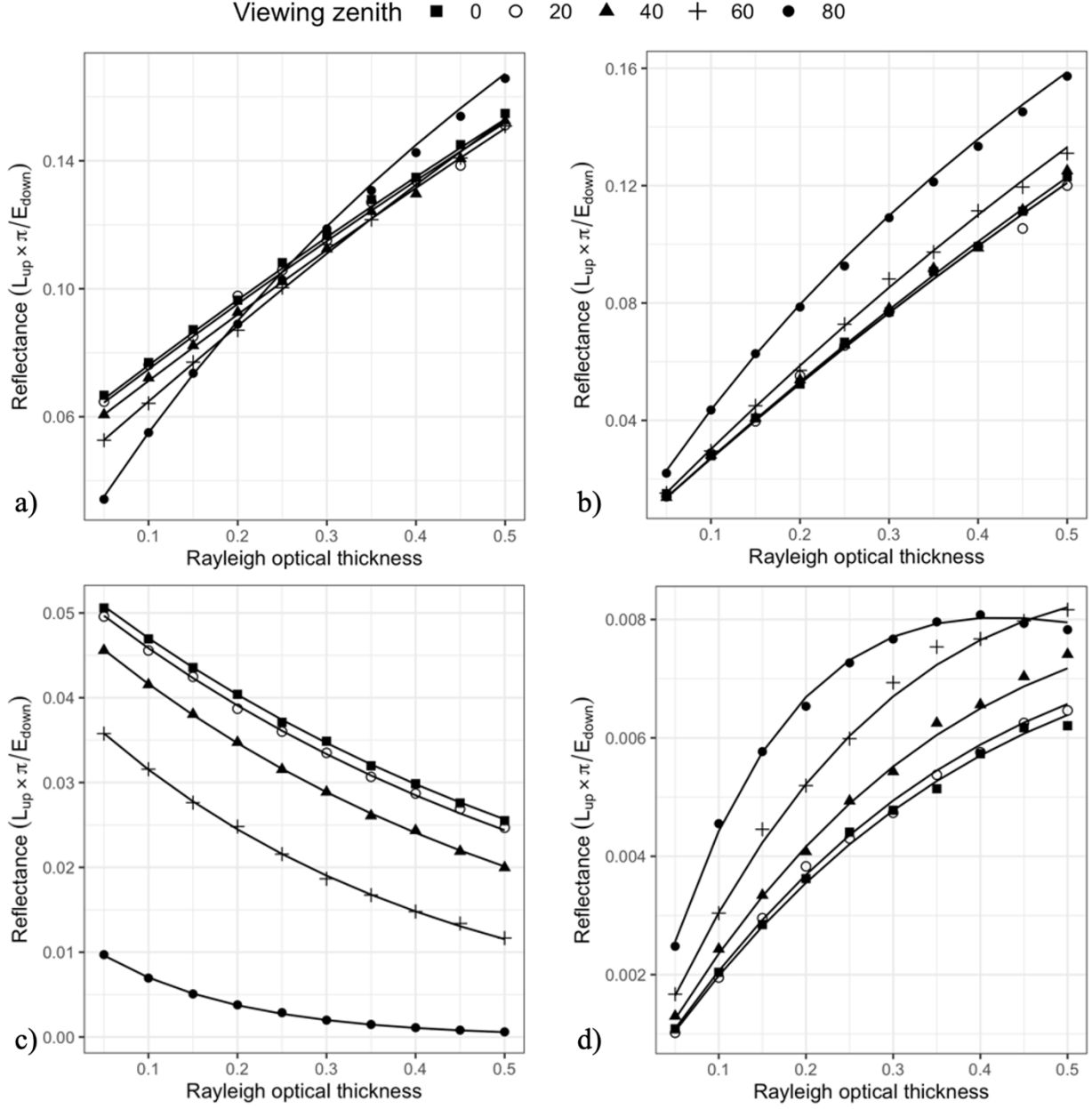| Solar zenith	Reflectance (E/E_0)	Irradiance (E/E_0)
0	0.159	0.214
20	0.019	0.162
40	0.030	-0.001
60	-0.003	0.085
80	-0.110	-0.076

Figure 11. a) Total, b) atmospheric intrinsic, c) direct and d) environmental reflectances at TOA as a function of molecular-scattering optical thickness at selected viewing zenith angles. Lines are from libRadtran DISORT, shapes are from T-Mart. Nadir solar angle, $R_{surf} = 0.1$, $N_{photon} = 10,000$, $\tau_{abs} = 0.3$.

The high-absorbance scenarios (Figures 9 to 11) generally share the same trend as the no-absorbance scenarios (Figures 6 to 8), with highly similar results between the two models when T-Mart runs with a million photons (Figure 6 and Figure 9) and noise with ten thousand photons (Figure 8 and Figure 11). For the one-million-photon runs, a maximum mean difference of 0.214% is found in the surface irradiance at a nadir solar angle (Table 5).

With 6S

6S (Vermote et al., 1997) is another RTE code widely used in the remote-sensing community. It solves RTEs with a method named successive order of scattering. Some quick comparisons were made between DISORT, T-Mart and 6S. It was found that the calculated TOA reflectances can be quite different between 6S and libRadtran (Figure 12). Notably, relative to libRadtran, 6S overestimates R_{atm} at small zenith angles (either solar or viewing while the other is 0, they give identical results because of the rule of reciprocity for R_{atm}) and underestimates R_{atm} at large zenith angles. T-Mart is not shown but it produces almost identical results as DISORT (Figure 6 and Figure 9).
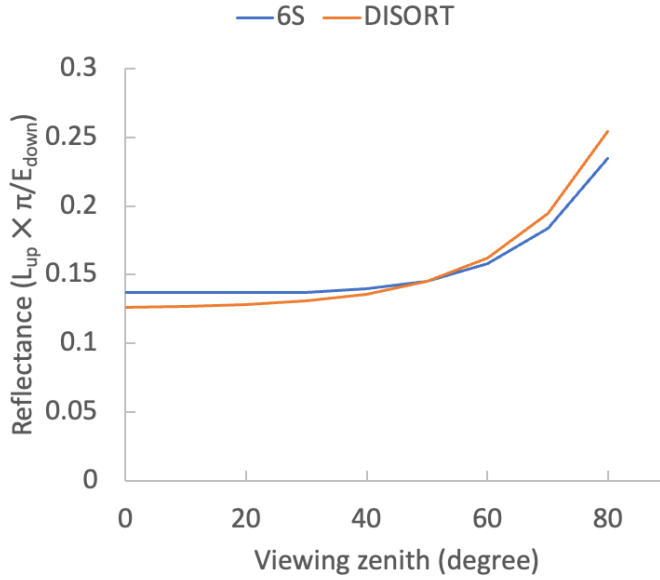

Figure 12. Atmospheric intrinsic reflectance calculated by 6S and DISORT at 400nm at various viewing zenith angles. Molecular-scattering optical thicknesses is 0.36, no absorption, no aerosols, nadir solar zenith angle.
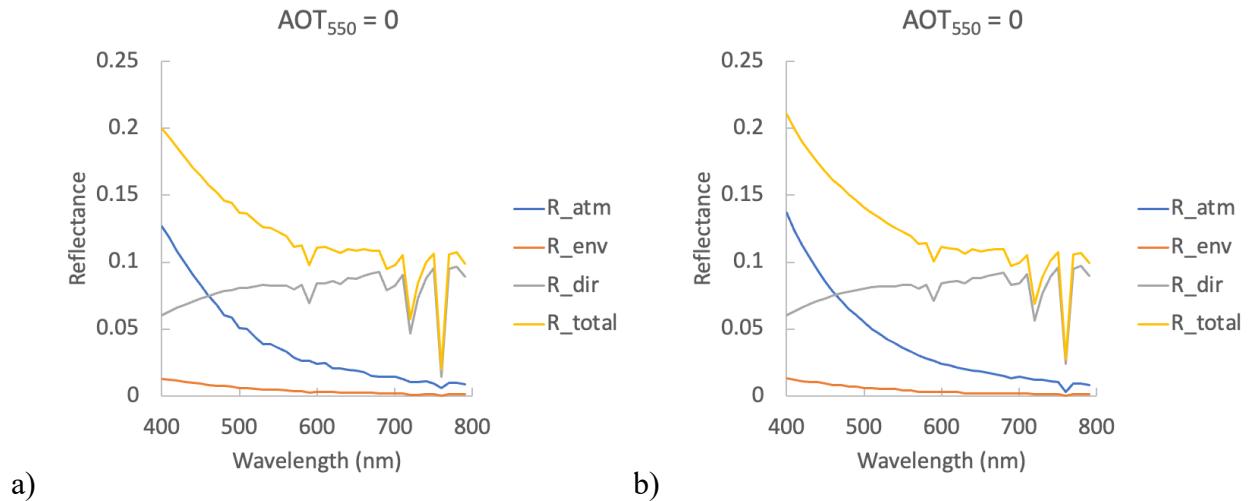

a)   b)

Figure 13. TOA reflectance of a Lambertian surface (R_{surf} = 0.1 at all wavelengths) calculated by a) T-Mart and b) 6S. Mid-latitude summer atmosphere and no aerosols. Nadir viewing and solar angles. N_{photon} = 10,000 for T-Mart.
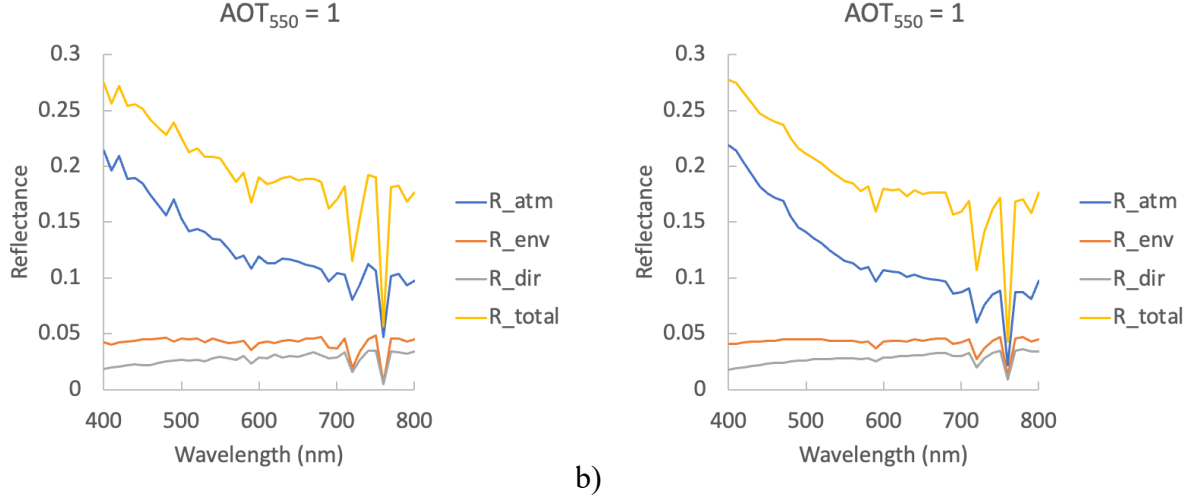

a)   b)

Figure 14. TOA reflectance of a Lambertian surface (R_{surf} = 0.1 at all wavelengths) calculated by a) T-Mart and b) 6S. Mid-latitude summer atmosphere. Maritime aerosols and AOT_{550} = 1. Nadir viewing and solar angles. N_{photon} = 10,000 for T-Mart.

Results from T-Mart and 6S generally align with each other, except at high-absorbance wavelengths such as 760nm (Figure 13 and Figure 14). The differences are less of a concern because these high-absorptance wavelengths are usually avoided for aquatic remote sensing. Note that an aerosol optical thickness at 550nm (AOT_{550}) of 1 is much higher than the molecular-scattering optical thickness in the modelled wavelengths, making it a major contributor to R_{atm} especially in longer wavelengths (Figure 14). The lowered R_{atm} from 6S between 600 and 800nm is likely due to overestimated absorption compared to libRadtran solvers and T-Mart.

Overall, T-Mart produces highly similar results as those from libRadtran DISORT (difference < 1% when N_{photon} = 1,000,000, Figure 7 and Figure 10), and it generally aligns well with 6S except at high-absorbance wavelengths (Figure 13 and Figure 14).

Preliminary Results

Now, with some confidence, we model the TOA reflectance of water using T-Mart, and see how coasts (with and without sloping terrain) affect the water's TOA reflectance. Although specular reflectance is included in T-Mart, it is not yet validated against other RTM codes; therefore, all surfaces are Lambertian in the preliminary results. This can lead to slight biases in water reflectances.
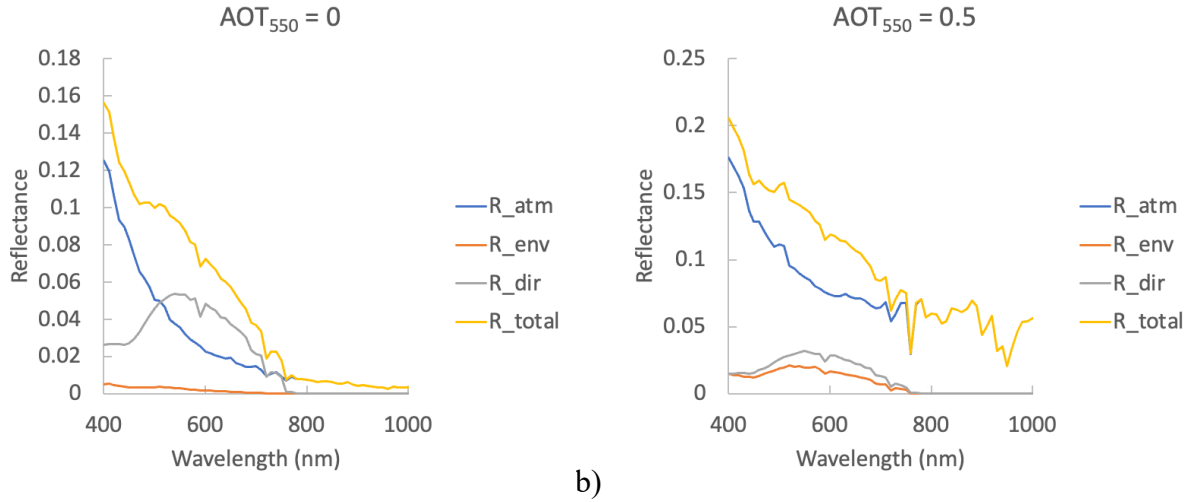
Figure 15. TOA reflectance of homogeneous water (see surface reflectance in Figure 4). Mid-latitude summer atmosphere. Maritime aerosols. AOT_{550} = a) 0 and b) 0.5. N_{photon} = 10,000.

In Figure 15 we can see that an AOT_{550} of 0.5 significantly increased the amount of environmental reflectance (orange lines). This makes sense because aerosol scattering is strongly forward scattering, contributing to photons travelling between the sun and the surrounding area of the target.
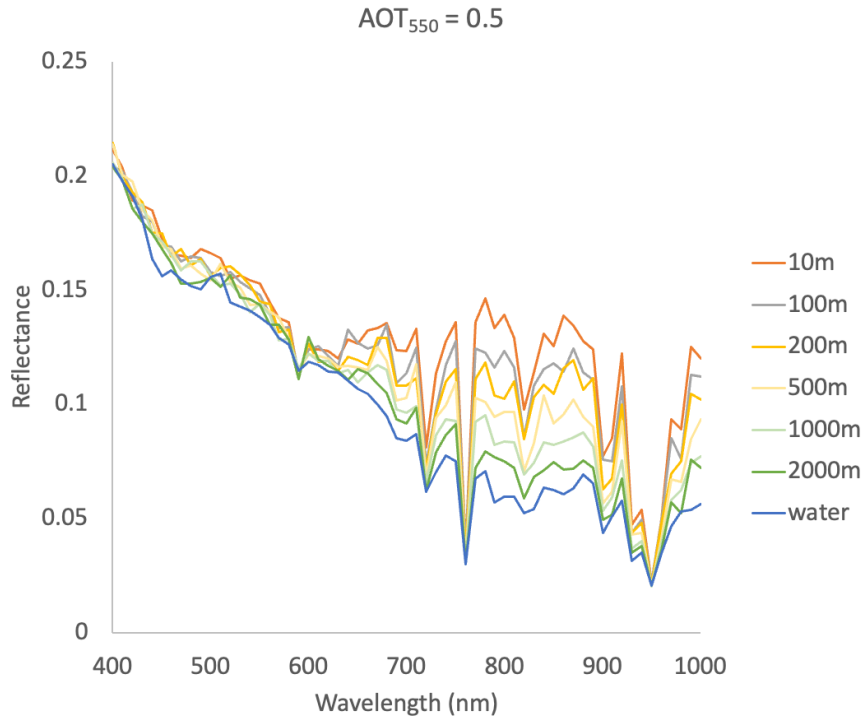

Figure 16. Total TOA reflectance of water as a function of distance from a straight coastline of vegetation (see surface reflectances in Figure 4). Mid-latitude summer atmosphere. Maritime aerosols. AOT_{550} = 0.5, Nadir viewing and solar angles, N_{photon} = 10,000.

The adjacency effect was examined by simulating TOA reflectances at different distances from a shoreline of vegetation (Figure 16). Compared to the reflectance of homogeneous water, coastal water exhibits significantly elevated TOA reflectance in the red and near-infrared wavelengths where vegetation has a high surface reflectance.

The scenario in Figure 16 was simulated again 10m from a shore with sloping coasts (Figure 17). It was run with a reduced spectral resolution to save computation time. The slopes are covered by vegetation and they extend to infinity. Surprisingly even with a slope that is almost vertical (80 degrees), the TOA reflectance of water was not heavily affected by the terrain with a maximum change of approximately 0.02 in reflectance (Figure 17b). This can likely be attributed to the increased R_{env} from the elevated shoreline of vegetation being offset by the decreased R_{atm} due to reduced space in the atmosphere.
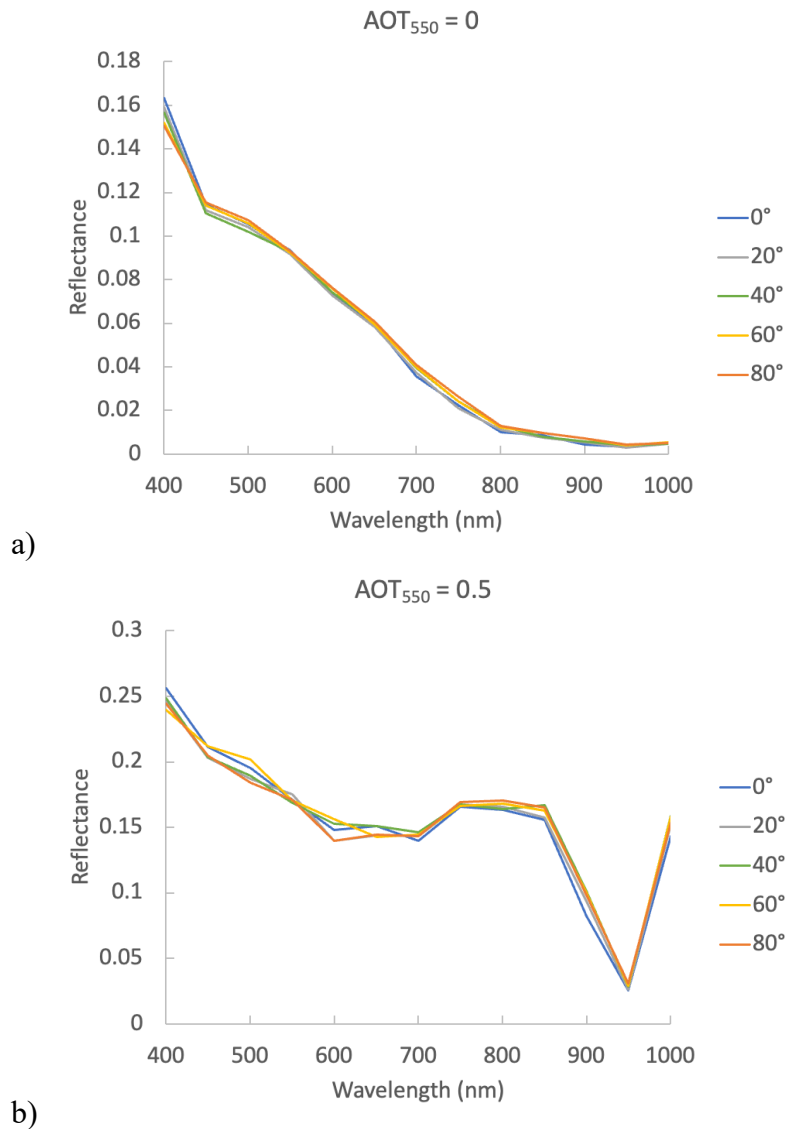

a)

b)

Figure 17. TOA reflectance of water 10m from a slope of vegetation that extends infinitely into the sky. Lines represent slope of various degrees. Maritime aerosols. AOT_{550} is a) 0 and b) 0.5.

Mid-latitude summer atmosphere. Solar and viewing angles are a) 0 and b) 30 degrees facing the slope.

Discussion

T-Mart generally produces results that are very similar to libRadtran DISORT under a variety of atmospheric conditions (Figure 6 and Figure 9). The small differences (maximum difference < 1%) are likely due to 1) inherent noise of Monte Carlo simulations and 2) the ways two methods calculate coupled scattering-absorption effects. In low-absorption scenarios (on which most aquatic remote sensing applications rely), T-Mart has a mean difference smaller than 0.1 % compared to libRadTran (Figure 4) and therefore suits the need for aquatic remote sensing. Noticeable noise is observed in T-Mart-simulated reflectances (Figure 8 and Figure 11) when the sample size is small in their runs; this will likely disappear when N_{photon} is increased (compare the noise in Figures 8 and 11 to Figures 6 and 9).

DISORT and T-Mart results can be quite different from those calculated by 6S. A maximum difference of approximately 10% is found at 400nm, the most strongly scattering wavelength of the visible spectrum (Figure 12). Nevertheless, we import atmospheric and aerosol profiles from 6S because they are well documented and used extensively in the literature. While both are freely available to the public, 6S is more widely used in the academic community than libRadtran (3,607 vs. 1,394 citations) likely because 6S was published earlier (6S in 1997 vs. libRadtran in 2005) and 6S is relatively easier to install and implement — libRadtran depends on several programming libraries that are not maintained anymore.

Significant statistical noise is observed in T-Mart-simulated reflectances with high aerosol loads (Figure 14 and Figure 16) and this is likely due to the strong forwarding scattering of aerosols. Although this can be reduced by increasing the number of simulated photons, there are techniques to reduce the noise by deliberately increasing the chance of scattering into the direction of the sensor (Buras & Mayer, 2011). The noise-reduction techniques should be investigated to reduce computation time.

A quick and simple modelling shows that the slope of a vegetation-covered coastline has limited influences on the TOA reflectance of water (Figure 17). This is partially caused by the spectral shapes of vegetation and water: their difference is small in shorter wavelengths where molecular scattering is strong, and in longer wavelengths where the difference in reflectance is more significant, molecular scattering is weak. Compared to vegetation, snow has high reflectance across the visible spectrum and therefore the slope of snow-covered coasts will likely have a greater effect on the TOA reflectance of water. More complex terrains, such as fjords with snow-covered coasts, should be modelled as an extreme scenario to explore the influence of terrain on the adjacency effect. In addition, specular reflectance is not included in the preliminary runs and it can be significant at high solar zenith angles (Figure 5). More analysis is needed to draw conclusions on the effects of topography on water's TOA reflectance.

Additional Work

Aerosol Profiles

In this study, the optical properties of aerosols, such as extinction coefficients and scattering phase functions, are imported from 6S because they are more well-documented in 6S than those used in libRadtran. However, T-Mart is more similar to libRadtran which fails to produce identical results as 6S (Figure 12). As a result, scattering caused by aerosols is not fully validated although it is highly likely correct because 1) molecular scattering is validated and molecular scattering shares an almost identical scattering process as aerosol scattering except with a different scattering phase function, and 2) with an extreme AOT_{550} of 1, T-Mart and 6S produced results that closely resemble each other (Figure 14).

To formally validate aerosol scattering and enhance T-Mart's credibility, the source code of libRadtran will be investigated to extract aerosol profiles. Comprehensive comparisons of aerosol scattering will be made between T-Mart and libRadtran.

Validating Specular Reflectance

The Cox-Munk slope distribution statistics and Fresnel reflectance are implemented in T-Mart, but their accuracy is not yet validated. Comparisons will be made with HydroLight, a widely recognized RTE code specializing in modelling optical properties of various waters. It uses the Cox-Munk statistics to construct random hexagonal patches of wind-blown sea surfaces and estimates the optical properties of the water surface through the random slopes (Mobley, 1994a). HydroLight is a commercial software package for which the Shallow Water Earth Observation Lab has a licence. It is the ideal benchmark to validate the specular-reflectance calculation of T-Mart.

Running More Scenarios

More simulations need to be run in complex environments such as rivers, fjords, and bays, all with a range of land cover types, as these are the areas that exhibit the strongest adjacency effect. Factors contributing to the adjacency effect that need to be examined include topography, distance from shore, shape of shoreline, and sun-sensor geometry. The validity of the flat-earth assumption (i.e., no terrain) implemented in most RTE codes (e.g., Bulgarelli et al., 2014; Vermote et al., 1997) can be assessed with T-Mart.

Due to the significant computational cost of triangle-collision detection, T-Mart can run with flat surface models to save computational time in scenarios where topography proves to have limited impact.

Plan: Adjacency-Effect Correction

Introduction

There is a limited number of image processors that correct for adjacency effects. Some existing processors such as Sen2Cor (Main-Knorn et al., 2017) have adjacency correction options in the user interface but lack publicly available descriptions of details steps. ATCOR (Richter, 1996) has a simple empirical adjacency correction that lacks the modelling of geometry and particle scattering phase functions. Operational adjacency-correction algorithms with detailed descriptions include the Modular Inversion and Processing System (Kiselev et al., 2015) and the SIMilarity Environment Correction (SIMEC) algorithm implemented in the iCOR processor (Sterckx et al., 2011).

SIMEC corrects for adjacency effects through a semi physics-based approach. It relies on the assumption that water's spectral shape in the near-infrared range is stable for a wide range of water biophysical properties, and any deviation from this shape is a result of adjacency effects or errors in atmospheric correction. It therefore iteratively removes a small portion of the average land reflectance in the scene from the reflectance of water pixels until all pixels follow the predetermined spectral shape. In case the shape cannot be reached, SIMEC removes all the edits and keeps the pixel reflectance as what it is after the atmospheric correction. This, in theory, works very well in coastal and inland environments with deep waters; however, bottom reflectance in shallow waters, extreme turbidity or algal bloom and sunglint can significantly deviate water's reflectance from the predetermined spectral shape. This hinders the application of SIMEC in imagery captured by instruments not designed for ocean-colour studies such as Landsat 8 OLI and Sentinel-2 MSI as the sensors are usually not maneuvered to minimize sunglint. Violation of SIMEC's assumption in shallow waters makes it not applicable in satellite-derived bathymetry which relies on the attenuation of photons as a function of water depth. A fully physics-based adjacency-correction method will likely overcome these challenges and improve aquatic remote sensing of coastal and inland waters.

The main challenge in physics-based adjacency correction methods is to derive the environment weights for neighbouring pixels in a wide range of conditions. Environment weights are defined as how much of the neighbouring pixel's surface reflectance contributes to the target pixel's TOA reflectance. The derivation has been done for heterogeneous surfaces in two dimensions (i.e. flat surface) in the literature. Environment weights from flat surfaces are derived in a number of publications through the use of Monte Carlo (Reinersman & Carder, 1995; Tanre et al., 1981; Vermote et al., 2006). The rest of this introduction section summarizes these three works, introduces the radiative transfer equations that describe environment weights, and outlines the objectives. The equations are essential for quantifying and correcting for adjacency effects. Notations and derivations generally follow the work of Sei (2007).

The TOA reflectance of an infinite homogeneous Lambertian surface is given by Chandrasekhar's formula (1960),

$$\rho_{toa} = \rho_{atm} + \frac{T^{\downarrow}T^{\uparrow}\rho_{Lamb}}{1 - S\rho_{Lamb}} \qquad \text{Eq. 21}$$

where ρ_{atm} is the atmospheric intrinsic reflectance, $T^{\downarrow}$ is the downward atmospheric transmittance, $T^{\uparrow}$ is the upward atmospheric transmittance, S is the spherical albedo and ρ_{Lamb} is the surface reflectance of a homogeneous surface. Dependences on wavelengths and sun-target-sensor geometry are omitted for simplicity.

Each of the two transmittances can be separated into direct and diffuse transmittances

$$T = e^{-\tau/\mu} + t \qquad \text{Eq. 22}$$

where τ is the optical depth, μ is the cosine of the zenith angle and t is the diffuse transmittance. Now Eq. 21 can be written as

$$\rho_{toa} = \rho_{atm} + \frac{T^{\downarrow}(e^{-\tau/\mu}\rho_{Lamb} + t^{\uparrow}\rho_{Lamb})}{1 - S\rho_{Lamb}} \qquad \text{Eq. 23}$$

When dealing with an inhomogeneous surface, the contribution of pixels surrounding the target pixel is replaced by an average reflectance $\langle\rho\rangle$ which accounts for the diffuse transmittance and multiple scattering part of the TOA signals. Eq. 23 becomes

$$\rho_{toa} = \rho_{atm} + \frac{T^{\downarrow}(e^{-\tau/\mu}\rho + t^{\uparrow}\langle\rho\rangle)}{1 - S\langle\rho\rangle} \qquad \text{Eq. 24}$$

where ρ is the surface reflectance of the target pixel. The average reflectance $\langle\rho\rangle$ can be noted as (Tanre et al., 1981; Vermote et al., 2006)

$$\langle\rho\rangle(x_0, y_0) = \int_{-\infty}^{+\infty}\int_{-\infty}^{+\infty} \rho(x_0 - x, y_0 - y)h(x,y)dxdy \qquad \text{Eq. 25}$$

where the point spread function $h(x,y)$ describes the amount of the neighbouring pixel's reflectance contributing to $\langle\rho\rangle$. It is a function of the linear distance between the target pixel and the environment pixel,

$$h(x,y) = \frac{f(\sqrt{x^2 + y^2})}{2\pi\sqrt{x^2 + y^2}} \qquad \text{Eq. 26}$$

where $f(r)$ is the derivative of the environment weighting function F, so $f(r) = F'(r)$. Various derivations of $F(r)$ exist in the literature. For example, Vermote et al. (1997) proposed the following solution for the 6S RTM code from Monte Carlo sampling,

$$F(r) = \frac{t_d^R F_R(r) + t_d^A F_A(r)}{t_d^R + t_d^A} \text{ with } t_d^R = e^{\frac{\tau_R}{2}} \text{ and } t_d^A = e^{\frac{5\tau_A}{6}} \qquad \text{Eq. 27}$$

$$F_R(r) = 1 - 0.930\,exp(-0.08r) - 0.070exp\,(-1.1r)$$

$$F_A(r) = 1 - 0.375\,exp(-0.2r) - 0.625exp\,(-1.83r)$$

where t_d^R is the diffuse Rayleigh transmittance, t_d^A is the diffuse aerosol transmittance, τ_R is the Rayleigh optical thickness and τ_A the aerosol optical thickness.

It is important to note that the environment weighting function F has values circularly symmetrical around the target pixel for a nadir viewing angle. In other words, when the viewing zenith angle is 0 and all the surfaces follow Lambertian reflectance, the environment weight of a neighbouring pixel is only a function of distance from the target pixel and there is no directional dependence. However, with a viewing zenith angle larger than 0, the environment weights are higher in pixels close to the sensor compared to pixels on the other side of the target pixel with the same distance from the target pixel (Vermote et al., 1997). This is confirmed by the modelling of Bulgarelli (2014) where adjacency effects are more prominent when the sensor is viewing a water pixel from above the land in a coastal environment as opposed to above the ocean. As a result, this solution in 6S does not work well for an arbitrary viewing geometry, not to mention the complex landscape morphology in coastal regions where adjacency effects are observed in aquatic remote sensing.

This study aims to expand Eq. 27 and derive a general form of environment weighting functions that considers complex sun-target-sensor geometry and landscape morphology for remote sensing of coastal and inland waters. The new environment weighting function can be used to correct for adjacency effects in complex environments. It will be packaged as a pre-processing tool for Sentinel-2 imagery that removes adjacency effects from water pixels. While the correction for adjacency effects from clouds is not planned, this study may use the spectral shape of water in near-infrared ranges to improve the overall accuracy (Sterckx et al., 2011).

Methodology

Overview

The environment weighting function above (Eq. 27) will be expanded to include a large number of variables (section 5.2.2). Using the new function, adjacency effects can be iteratively removed from every water pixel of a satellite or airborne image.

Ideally, the algorithm takes in an image of TOA reflectance, the corresponding DEM and the atmospheric conditions as input, and outputs an image with adjacency effects removed for water pixels. The output can be either surface reflectance or TOA reflectance, the latter facilitates the use of other atmospheric-corrections tools at the user's choice.

Creating Simulated Data

The model proposed in paper 1 will be run a large number of times to derive environment weights for neighbouring pixels of different conditions, the variables include

- Distance between the neighbouring pixel and the target pixel
- Relative position of the two pixels
- Elevation and slope of the neighbouring pixel
- Sun-target-sensor geometry
- Slope and its direction relative to viewing and solar geometry
- Atmospheric conditions: scattering and absorption by gases and aerosols
- Wavelength of light

Deriving Environment Weights

An environment weighting function will be derived from regressions of simulated environment weights and the variables in Section 5.2.2 through machine learning and neural network approaches. The results will either be analytical expressions or a look-up table.

Computational Optimization

To reduce computation time, instead of looping through every neighbouring pixel in the range with noticeable environment weights, a method that groups neighbouring pixels into spider-web-shape subsets can be applied. The subsets far from the target pixel will have larger areas and more pixels therefore are more affected by heterogeneity, but this will be partially balanced by the fact the environment weights decrease exponentially with distance.

Validation

The robustness of this adjacency-correction algorithm can be validated with in-situ aquatic spectral data from the South Nation and AERONET-OC sites. Secondarily it can also be validated with existing water-depth data to see if adjacency correction improves the accuracy of satellite-derived bathymetry. Transecting/Profiling the reflectance of sizable inland waterbodies such as Lake Simcoe and the Great Lakes can also function as validation data.

If the corrected TOA reflectance of a pixel satisfies the assumption that the surface is homogeneous (i.e., no adjacency effects present), then in theory the surface reflectance of this pixel can be used to produce the same TOA reflectance for validation. This can be easily done in 6S.

If the assumption of deep water is valid and in the absence of sunglint, the retrieved surface reflectance can be compared with the predetermined reflectance spectrum of natural waters in the near-infrared range (Sterckx et al., 2011).

References

Bulgarelli, B., Kiselev, V., & Zibordi, G. (2014). Simulation and analysis of adjacency effects in coastal waters: A case study. *Applied Optics*, *53*(8), 1523. https://doi.org/10.1364/AO.53.001523

Bulgarelli, B., & Zibordi, G. (2018). On the detectability of adjacency effects in ocean color remote sensing of mid-latitude coastal environments by SeaWiFS, MODIS-A, MERIS, OLCI, OLI and MSI. *Remote Sensing of Environment*, *209*, 423–438. https://doi.org/10.1016/j.rse.2017.12.021

Buras, R., & Mayer, B. (2011). Efficient unbiased variance reduction techniques for Monte Carlo simulations of radiative transfer in cloudy atmospheres: The solution. *Journal of Quantitative Spectroscopy and Radiative Transfer*, *112*(3), 434–447. https://doi.org/10.1016/j.jqsrt.2010.10.005

Chandrasekhar, S. (1960). *Radiative Transfer*. Dover Publications.

Cox, C., & Munk, W. (1954). Measurement of the Roughness of the Sea Surface from Photographs of the Sun's Glitter. *Journal of the Optical Society of America*, *44*(11), 838. https://doi.org/10.1364/JOSA.44.000838

Ehret, G., Kiemle, C., Wirth, M., Amediek, A., Fix, A., & Houweling, S. (2008). Space-borne remote sensing of CO2, CH4, and N2O by integrated path differential absorption lidar: A sensitivity analysis. *Applied Physics B-Lasers and Optics*, *90*(3–4), 593–608. https://doi.org/10.1007/s00340-007-2892-3

Emde, C., Buras-Schnell, R., Kylling, A., Mayer, B., Gasteiger, J., Hamann, U., Kylling, J., Richter, B., Pause, C., Dowling, T., & Bugliaro, L. (2016). The libRadtran software package for radiative transfer calculations (version 2.0.1). *Geoscientific Model Development*, *9*(5), 1647–1672. https://doi.org/10.5194/gmd-9-1647-2016

Frouin, R., Schwindling, M., & Deschamps, P.-Y. (1996). Spectral reflectance of sea foam in the visible and near-infrared: In situ measurements and remote sensing implications. *Journal of Geophysical Research: Oceans*, *101*(C6), 14361–14371. https://doi.org/10.1029/96JC00629

Gordon, H. R. (1985). Ship perturbation of irradiance measurements at sea 1: Monte Carlo simulations. *Applied Optics*, *24*(23), 4172. https://doi.org/10.1364/AO.24.004172

Hedley, J., Russell, B., Randolph, K., & Dierssen, H. (2016). A physics-based method for the remote sensing of seagrasses. *Remote Sensing of Environment*, *174*, 134–147. https://doi.org/10.1016/j.rse.2015.12.001

Kiselev, V., Bulgarelli, B., & Heege, T. (2015). Sensor independent adjacency correction algorithm for coastal and inland water systems. *Remote Sensing of Environment*, *157*, 85–95. https://doi.org/10.1016/j.rse.2014.07.025

Kutser, T., Hedley, J., Giardino, C., Roelfsema, C., & Brando, V. E. (2020). Remote sensing of shallow waters – A 50 year retrospective and future directions. *Remote Sensing of Environment*, *240*, 111619. https://doi.org/10.1016/j.rse.2019.111619

Lee, Z., Carder, K. L., Mobley, C. D., Steward, R. G., & Patch, J. S. (1998). Hyperspectral remote sensing for shallow waters I A semianalytical model. *Applied Optics*, *37*(27), 6329. https://doi.org/10.1364/AO.37.006329

Light, B. (2003). A two-dimensional Monte Carlo model of radiative transfer in sea ice. *Journal of Geophysical Research*, *108*(C7), 3219. https://doi.org/10.1029/2002JC001513

Main-Knorn, M., Pflug, B., Louis, J., Debaecker, V., Müller-Wilm, U., & Gascon, F. (2017). Sen2Cor for Sentinel-2. In L. Bruzzone, F. Bovolo, & J. A. Benediktsson (Eds.), *Image and Signal Processing for Remote Sensing XXIII* (p. 3). SPIE. https://doi.org/10.1117/12.2278218

Marchuk, G. I., Mikhailov, G. A., Nazareliev, M. A., Darbinjan, R. A., Kargin, B. A., & Elepov, B. S. (1980). *The Monte Carlo Methods in Atmospheric Optics*. Springer-Verlag. https://doi.org/10.1007/978-3-540-35237-2

Mayer, B. (2009). Radiative transfer in the cloudy atmosphere. *The European Physical Journal Conferences*, *1*, 75–99. https://doi.org/10.1140/epjconf/e2009-00912-1

Mayer, B., & Kylling, A. (2005). Technical note: The libRadtran software package for radiative transfer calculations – description and examples of use. *Atmos. Chem. Phys.*, 23.

Mobley, C. D. (1994a). Chapter 4 Across the Surface. In *Light and Water: Radiative Transfer in Natural Waters*.

Mobley, C. D. (1994b). Chapter 6 Monte Carlo Methods. In *Light and Water: Radiative Transfer in Natural Waters*.

Mobley, C. D. (2020). *Absorption by Oceanic Constituents: Ocean Optics Web Book*. Ocean Optics Web Book. https://oceanopticsbook.info/view/absorption/absorption-by-oceanic-constituents

Mobley, C. D. (2021a). *Cox-Munk Sea Surface Slope Statistics*. Ocean Optics Web Book. https://oceanopticsbook.info/view/surfaces/cox-munk-sea-surface-slope-statistics

Mobley, C. D. (2021b). *The Atmospheric Correction Problem*. Ocean Optics Web Book. https://www.oceanopticsbook.info/view/atmospheric-correction/the-atmospheric-correction-problem

Mobley, C. D. (2021c). *The Level Sea Surface*. Ocean Optics Web Book. https://oceanopticsbook.info/view/surfaces/the-level-sea-surface

Mobley, C. D. (2021d). *Whitecaps*. Ocean Optics Web Book. https://oceanopticsbook.info/view/atmospheric-correction/level-2/whitecaps

Mobley, C. D., & Sundman, L. K. (2008). *Hydrolight 5 Ecolight 5 Technical documentation*. Bellevue, WA: Sequoia Scientific Inc.

Moses, W. J., Sterckx, S., Montes, M. J., De Keukelaere, L., & Knaeps, E. (2017). Atmospheric Correction for Inland Waters. In *Bio-optical Modeling and Remote Sensing of Inland Waters* (pp. 69–100). Elsevier. https://linkinghub.elsevier.com/retrieve/pii/B9780128046449000033

Palmer, S. C. J., Kutser, T., & Hunter, P. D. (2015). Remote sensing of inland waters: Challenges, progress and future directions. *Remote Sensing of Environment*, *157*, 1–8. https://doi.org/10.1016/j.rse.2014.09.021

Reinersman, P. N., & Carder, K. L. (1995). Monte Carlo simulation of the atmospheric point-spread function with an application to correction for the adjacency effect. *Applied Optics*, *34*(21), 4453. https://doi.org/10.1364/AO.34.004453

Richter, R. (1996). A spatially adaptive fast atmospheric correction algorithm. *International Journal of Remote Sensing*, *17*(6), 1201–1214. https://doi.org/10.1080/01431169608949077

Saleh, R., Marks, M., Heo, J., Adams, P. J., Donahue, N. M., & Robinson, A. L. (2015). Contribution of brown carbon and lensing to the direct radiative effect of carbonaceous aerosols from biomass and biofuel burning emissions. *Journal of Geophysical Research-Atmospheres*, *120*(19), 10285–10296. https://doi.org/10.1002/2015JD023697

Sei, A. (2007). Analysis of adjacency effects for two Lambertian half-spaces. *International Journal of Remote Sensing*, *28*(8), 1873–1890. https://doi.org/10.1080/01431160600851868

Sei, A. (2015). Efficient correction of adjacency effects for high-resolution imagery: Integral equations, analytic continuation, and Padé approximants. *Applied Optics*, *54*(12), 3748. https://doi.org/10.1364/AO.54.003748

SEOS. (n.d.). *Introduction to Remote Sensing*. Retrieved August 7, 2021, from https://seos-project.eu/remotesensing/remotesensing-c01-p06.html

Sterckx, S., Knaeps, E., & Ruddick, K. (2011). Detection and correction of adjacency effects in hyperspectral airborne data of coastal and inland waters: The use of the near infrared similarity spectrum. *International Journal of Remote Sensing*, *32*(21), 6479–6505. https://doi.org/10.1080/01431161.2010.512930

Tanre, D., Herman, M., & Deschamps, P. Y. (1981). Influence of the background contribution upon space measurements of ground reflectance. *Applied Optics*, *20*(20), 3676. https://doi.org/10.1364/AO.20.003676

Vermote, E., Tanre, D., Deuze, J. L., Herman, M., & Morcrette, J.-J. (1997). Second Simulation of the Satellite Signal in the Solar Spectrum, 6S: An overview. *IEEE Transactions on Geoscience and Remote Sensing*, *35*(3), 675–686. https://doi.org/10.1109/36.581987

Vermote, E., Tanré, D., Deuze, J. L., Herman, M., & Morcrette, J.-J. (2006). *Second Simulation of a Satellite Signal in the Solar Spectrum—Vector (6SV)*. 6S User Guide Version 3.

Wilson, R. T. (2013). Py6S: A Python interface to the 6S radiative transfer model. *Computers & Geosciences*, *51*, 166–171. https://doi.org/10.1016/j.cageo.2012.08.002